Article

Atmospheric molecular blobs shape up circumstellar envelopes of AGB stars

L. Velilla-Prieto[1✉], J. P. Fonfría[2], M. Agúndez[1], A. Castro-Carrizo[3], M. Guélin[3], G. Quintana-Lacaci[1], I. Cherchneff[4], C. Joblin[5], M. C. McCarthy[6], J. A. Martín-Gago[7] & J. Cernicharo[1✉]

During their thermally pulsing phase, asymptotic giant branch (AGB) stars eject material that forms extended dusty envelopes[1]. Visible polarimetric imaging found clumpy dust clouds within two stellar radii of several oxygen-rich stars[2–6]. Inhomogeneous molecular gas has also been observed in multiple emission lines within several stellar radii of different oxygen-rich stars, including W Hya and Mira[7–10]. At the stellar surface level, infrared images have shown intricate structures around the carbon semiregular variable R Scl and in the S-type star π^1 Gru[11,12]. Infrared images have also shown clumpy dust structures within a few stellar radii of the prototypical carbon AGB star IRC+10°216 (refs. [13,14]), and studies of molecular gas distribution beyond the dust formation zone have also shown complex circumstellar structures[15]. Because of the lack of sufficient spatial resolution, however, the distribution of molecular gas in the stellar atmosphere and the dust formation zone of AGB carbon stars is not known, nor is how it is subsequently expelled. Here we report observations with a resolution of one stellar radius of the recently formed dust and molecular gas in the atmosphere of IRC+10°216. Lines of HCN, SiS and SiC_2 appear at different radii and in different clumps, which we interpret as large convective cells in the photosphere, as seen in Betelgeuse[16]. The convective cells coalesce with pulsation, causing anisotropies that, together with companions[17,18], shape its circumstellar envelope.

The circumstellar envelope of IRC+10°216, the archetypal, high-mass-loss-rate carbon asymptotic giant branch (AGB) star that is also closest to the Sun, was observed with the Atacama large-millimetre array (ALMA) interferometer. These observations spatially resolved the region between 1 and 5 R_* (that is, roughly 20–100 mas, where R* is the stellar radius) with a spatial resolution of 27 × 19 mas. Further details on observations and data processing can be found in Methods. The continuum emission map at 1.2 mm wavelength (Fig. 1) shows resolved extensions (above 10 σ) that depart from spherical symmetry, in addition to a bright central source (Methods). A horseshoe-shaped structure is seen approximately 25 mas from the centre of the bright central source (see residuals map in Fig. 1). This structure extends from west to south, counterclockwise, and its size is comparable to the size of the star and also comparable to the size of predicted convective cells in the upper atmosphere of AGBs[19]. Two other continuum extensions appear further out in Fig. 1. These are located at approximately 90 mas northeast and 105 mas northwest from the continuum centre and could be either dusty gas clumps expelled by IRC+10°216 or dust-embedded (sub)stellar companions[20,21]. We note that such moving clumps have previously been reported in IRC+10°216 and other AGB stars, which we discuss in Methods.

In regard to molecular gas, the various molecular species that form show varied and strikingly asymmetric distributions. Figure 2 shows the continuum-subtracted circumstellar emission of SiC_2, SiS and HCN in the atmosphere of IRC+10°216 (see also Extended Data Figs. 1 and 2). The maps show, at the position of the star, a void of the size of the radio photosphere that is approximately 40 mas in radius[22]. This void is not due to the absence of gas in front of the star but to absorption by foreground gas (Methods). The line emission arising near the star, which involves upper-level energies up to some 6,500 K, clearly deviates from the circular symmetry we would expect in an isotropic formation scenario. In particular, emission is almost absent in the Western hemisphere of the envelope for the SiC_2 line and the unidentified feature centred at 251,123 MHz (U251123) shown in Fig. 2. Such an asymmetric pattern is commonly observed for other molecular species and takes the form of compact structures and clumps, as well as of emission gaps. The SiS $v = 3, J = 14–13$ emission in the central channels shown in Fig. 2 shows a very specific pattern of bright spots located north, east, south and west of the star. The HCN $v_3 = 1$ emission, also shown in Fig. 2, shows incomplete arc-like structures that resemble those seen at much larger scales (Fig. 3).

Accordingly, both molecular and dust emissions show a marked departure from spherical symmetry. Outside the central region where absorption in front of the stellar continuum occurs, the emission gaps shown in Fig. 2 for SiC_2 correspond to regions where average density, fractional abundances and temperatures do not meet the required

[1]Department of Molecular Astrophysics, Instituto de Física Fundamental, Madrid, Spain. [2]Centro de Astrobiología, CSIC-INTA, Villanueva de la Cañada, Spain. [3]Institut de Radioastronomie Millimétrique, Saint Martin d'Hères, France. [4]Departement Physik, Universität Basel, Basel, Switzerland. [5]Institut de Recherche en Astrophysique et Planétologie, Université Toulouse 3 – Paul Sabatier, CNRS, CNES, Toulouse, France. [6]Harvard-Smithsonian Center for Astrophysics, Cambridge, MA, USA. [7]Group of Structure of Nanoscopic Systems, Instituto de Ciencia de Materiales de Madrid, Cantoblanco, Spain. ✉e-mail: l.velilla@csic.es; jose.cernicharo@csic.es
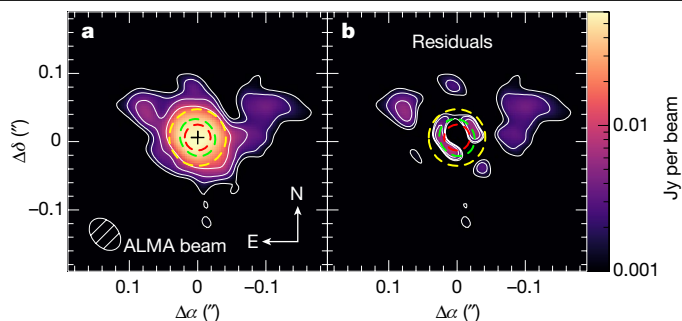
Fig. 1 | Continuum emission of IRC+10°216 at 1 mm. a, High-resolution image of the 1 mm continuum emission of IRC+10°216. The contour levels are at 10, 20, 40 and 100 σ, where σ is the r.m.s. of the noise and equal to 92 µJy per beam. The central cross and green dashed contour represent the centroid and full width at half-maximum (FWHM), respectively, of the Gaussian fit to the bulk of the emission. The red contour, centred at the position of our estimated Gaussian centroid, shows photosphere size in the near infrared[33,34]. The yellow contour shows the radio photosphere size at 7 mm from the analysis of high-resolution, Very Large Array (VLA) observations[22]. **b**, Map of the residuals of the fit.

conditions for production of detectable molecular emission. They hardly may be explained in a scenario of isotropic mass loss. This anisotropy in the formation of dust grains and molecules very probably occurs as a consequence of localized production of matter due to combined pulsation and large-scale convective motions in the photosphere of the star, as suggested by Weigelt et al.[23] and predicted by hydrodynamic models[19,24]. Episodes of asymmetric ejection of material, leading to the formation of dust clumps in the stellar photosphere of the Red Supergiant star Betelgeuse, have also been proposed to explain its recent Great Dimming[16]. Montargès et al.[16] argued that Betelgeuse ejected a bubble of gas some time before the Great Dimming as a consequence of stellar pulsation in the presence of giant convective cells, which turned into rapid dust formation once the temperature had dropped below condensation temperature. Similarly, we argue that we are witnessing the anisotropic formation of dust and molecular gas in the high-mass-loss-rate AGB star IRC+10°216 due to temperature and density anisotropies caused by large convective cells interacting with stellar pulsation-driven wind[25].

To gain more insight into the causes of the anisotropies observed for HCN and SiS, we compared the intensity ratio distribution between lines SiS $v = 3$, $J = 14–13$ and HCN $v_3 = 1$, $J = 3–2$ (Fig. 4). Although both lines have similar upper-level energy (3,281 and 3,042 K for SiS and HCN,
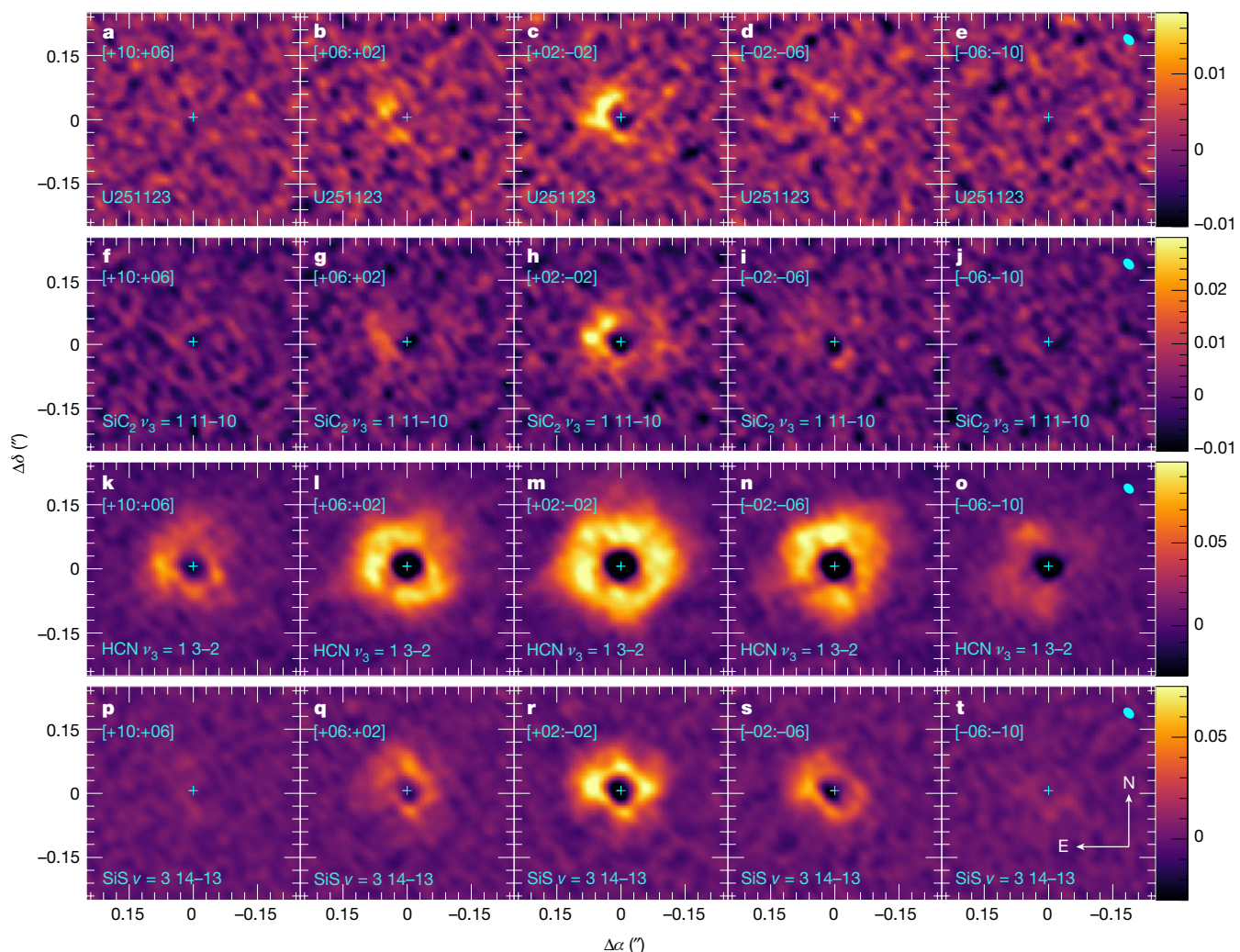

Fig. 2 | Velocity-integrated maps of different emission lines. a–e, Unidentified line U251123 (centroid at 251,123 MHz). **f–j**, SiC$_2$ $v_3 = 1$, $J_{k,k} = 11_{9,3}–10_{9,2}$. **k–o**, HCN $v_3 = 1$, $J = 3–2$. **p–t**, SiS $v = 3$, $J = 14–13$. **a,f,k,p**, [+10:+06]; **b,g,l,q**, [+01:+02]; **c,h,m,r**, [+02:−02]; **d,i,n,s**, [+02:−0.6]; **e,j,o,t**, [−0.6:−10]. The velocity range where the line has been integrated is shown in the top left corner of each box, in km s^{-1}.

Velocities are relative to the systemic velocity of the source in the LSR (Local Standard of Rest)—that is, −26.5 km s^{-1} (ref. [20]). **e,j,o,t**, The size and shape of the synthetic beam for each line are shown in the top right corner. The cross in cyan at the centre represents the position of the peak of the Gaussian fit of the continuum. North is up, east is to the left, as shown in **t**.
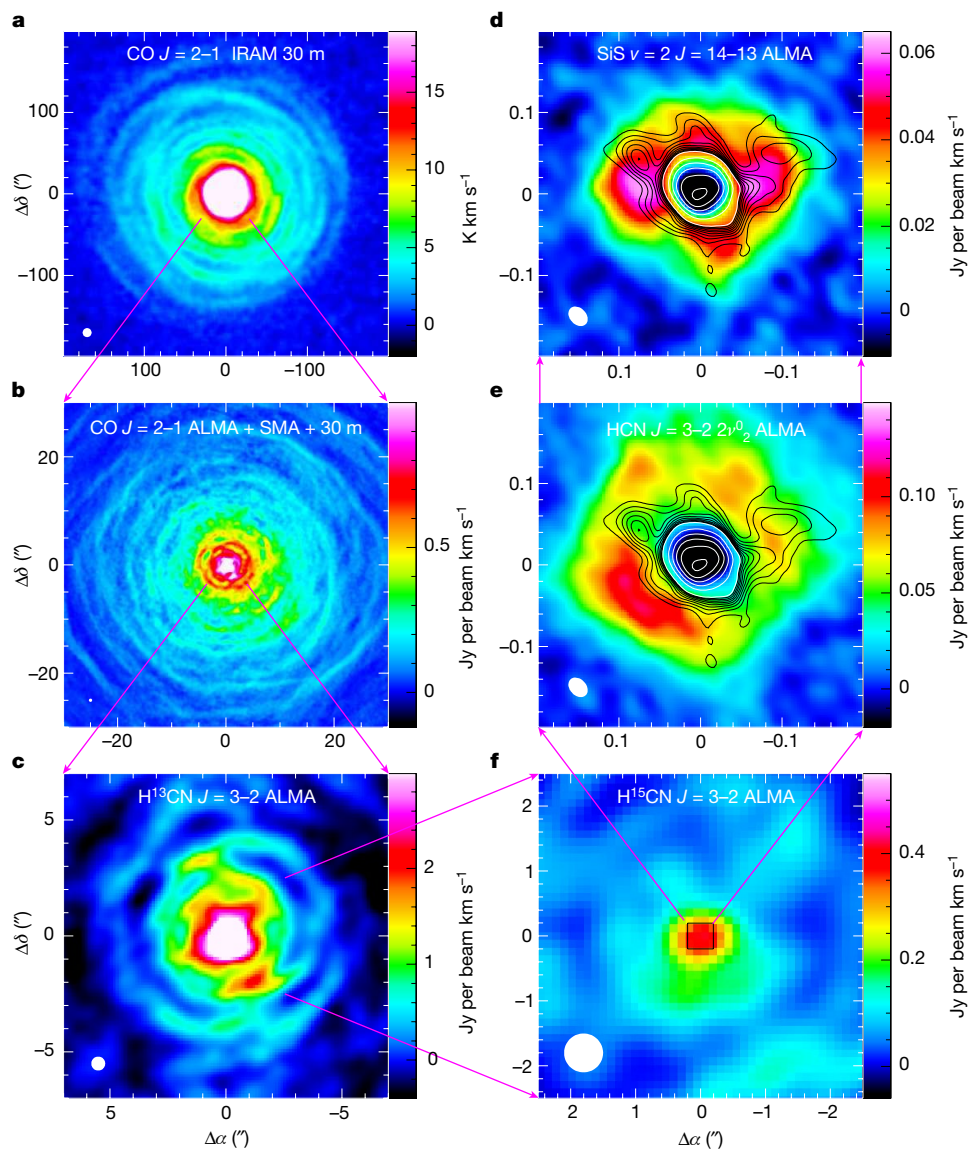
Fig. 3 | Velocity-integrated emission maps of the circumstellar environment of IRC+10°216 for different molecules. a, CO $J = 2–1$ IRAM 30 m. **b**, CO $J = 21$ ALMA + SMA + 30 m. **c**, $H^{13}CN J = 3–2$ ALMA. **d**, SiS $v = 2 J = 14–13$ ALMA. **e**, HCN $J = 3–2 2v_2^0$ ALMA. **f**, $H^{15}CN J = 3–2$ ALMA. From the largest scales shown (**a**,**b**)[20,29], we progressively zoom into the central emission down to scales comparable to a few stellar radii (**e**,**f**). Different telescopes were used to observe the source: the Institute de Radioastronomie Millimétrique (IRAM) 30 m telescope, the Submillimetre Array (SMA) and ALMA. Spatial resolution is shown as a white ellipse in the bottom-left corner of each panel. **e**,**f**, Black and white contours represent, respectively, continuum emission at levels from 1 to 10 mJy in steps of 1 mJy and from 10 up to 60 mJy in steps of 10 mJy; 1 mJy is approximately equal to 10 σ (Fig. 1). North is up, east is to the left.

respectively), there are large angular variations in their intensity ratio at a given distance from the star. In particular, the HCN: SiS ratio is strongly enhanced at position angles (PAs) 140, 250 and 340°—that is, southeast, southwest and northwest. The fact that, for a given radius, the HCN:SiS line ratio undergoes such angular variations implies that anisotropies in the emission are not solely due to line excitation changes caused by fluctuations in gas density, in which case the fractional abundances of both HCN and SiS would change equally and the ratio would not vary with angle. It is likely that they resulted from anisotropies in the temperature that weight differently on the fractional abundances of HCN and SiS. Such behaviour is predicted by chemical equilibrium models (results in Extended Data Figs. 3 and 4 and description in Methods). We note that chemical equilibrium models effectively predict enhanced sensitivity of the chemical composition to the temperature at the photosphere, where temperature and pressure are very high, whereas shocks models remain inherently uncertain due to both high sensitivity to the

underlying physical structure and incompleteness of the chemical kinetics network. This incompleteness relates to the limited knowledge of formation and destruction chemical routes, the restricted database of available reactions rates and the range of explored temperatures. Our chemical equilibrium models indicate that the formation of each molecule is favoured over a given pressure–temperature domain. For example, a temperature increase reduces SiS abundance more markedly than for HCN. Even a moderate variation of 10% in temperature among different regions of the stellar atmosphere can lead to orders of magnitude variation in the fractional abundances of molecules such as HCN and SiS, as well as of dust precursors such as C_2 and SiC_2 (Extended Data Fig. 3). Laboratory simulations have shown that the chemistry of C and C_2 in the presence of H_2 leads to the growth of carbon clusters and the formation of amorphous carbon nanoparticles[26]. On the other hand, SiC_2 is suspected of being a precursor in the formation of silicon carbide[27]. Phenomena such as large convection cells at the surface of
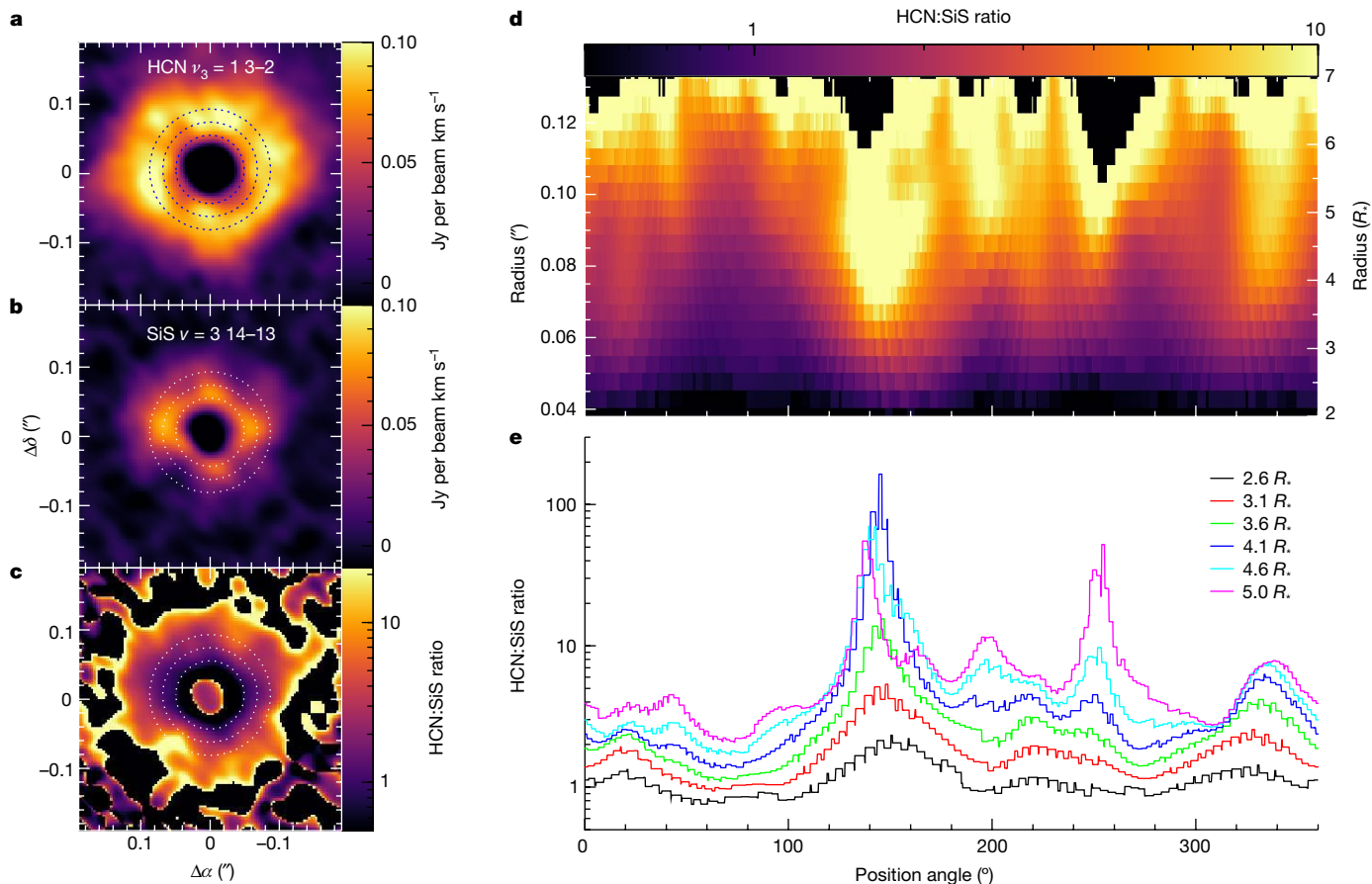
Fig. 4 | Analysis of intensity ratio of emission lines HCN $v_3 = 1$, $J = 3-2$ and SiS $v = 3$, $J = 14-13$. a,b, Velocity-integrated emission maps HCN $v_3 = 1$, $J = 3-2$ (**a**) and SiS $v = 3$, $J = 14-13$ (**b**) of within ± 2 km s^{-1} from the systemic velocity of the source. **c,** Map of the intensity ratio between these lines, where the colour scale is logarithmic for enhanced visualization. **a**–**c,** Dotted circles correspond to distances of 2.5, 3.5 and 4.5 stellar radii assuming a 19 mas radius[33]. **d,** Rectangular projection (position angle versus distance) of the HCN:SiS intensity ratio map to improve visualization of variation in the ratio at different distances. **e,** Curves of intensity ratio at six different distances from the star.

the star that add up to pulsation-driven wind should produce variations in the temperature with angle, which in turn cause fractional abundance gradients and ultimately lead to the anisotropies seen in molecular emission.

Alternative scenarios considered to explain the asymmetries observed in IRC+10°216 are the effect of a binary companion and shocks in the atmosphere of the star. IRC+10°216 is very probably part of a multiple star system that shapes up the characteristic shell structure of its outer envelope. Its orbital period or periods has, or have, been estimated by different authors at approximately 700 and 50 years[20,28,29]. However, the structures we see at atmospheric scales are only 2–4 years old, much too young to invoke gravitational pull by any companion star or planet. Moreover, manifestations of the binary interaction affecting close circumstellar environments are not observed in our maps, such as a disk or a torus-like structure or preferred ejection directions. Photochemical effects enhanced by the ultraviolet emission of a close companion, as recently studied by Siebert et al.[15], cannot explain the asymmetries we observed at atmospheric level in the brightness distribution of either SiS or HCN, because several emission voids surround the star. We also found no evidence of shocks, which would have left signatures in the emission maps such as infalling material and narrow velocity features in the emission profiles (Methods, see also Extended Data Figs. 5, 6, 7, 8 and 9). Nevertheless, we cannot rule out the existence of shocks which, in any case, should be triggered by the stellar pulsation and convective motions in the photosphere[25]. Further discussion about alternative scenarios and models considering the combination of

anisotropic mass loss and binary interaction are presented in Methods (see also Extended Data Fig. 10).

The anisotropies reported here change our views on the formation of molecules and dust in the upper atmosphere of the archetypal AGB star IRC+10°216, with different molecular species selectively appearing depending on local physical conditions. Conversely, this is of critical importance in regard to the mechanisms that later drive the winds of intermediate mass stars and the ensuing circumstellar chemistry[30–32]. We conclude that, independently of the effect of a binary companion in reshaping the outer circumstellar envelope, the molecular and dust anisotropies observed in IRC+10°216—and presumably present in most late-type stars—lead to the formation of physical structures that, expanding with stellar wind, shape up the global spatial structure and evolution of the envelope.

Online content

Any methods, additional references, Nature Portfolio reporting summaries, source data, extended data, supplementary information, acknowledgements, peer review information; details of author contributions and competing interests; and statements of data and code availability are available at https://doi.org/10.1038/s41586-023-05917-9.

1. Habing, H. J. & Olofsson, H. *Asymptotic Giant Branch Stars* (Springer, 2004).
2. Adam, C. & Ohnaka, K. Exploring the innermost dust formation region of the oxygen-rich AGB star IK Tauri with VLT/SPHERE-ZIMPOL and VLTI/AMBER. *Astron. Astrophys.* **628**, A132 (2019).

Article

3. Khouri, T. et al. Study of the inner dust envelope and stellar photosphere of the AGB star R Doradus using SPHERE/ZIMPOL. *Astron. Astrophys.* **591**, A70 (2016).
4. Khouri, T. et al. Inner dusty envelope of the AGB stars W Hydrae, SW Virginis, and R Crateris using SPHERE/ZIMPOL. *Astron. Astrophys.* **635**, A200 (2020).
5. Ohnaka, K., Weigelt, G. & Hofmann, K.-H. Clumpy dust clouds and extended atmosphere of the AGB star W Hydrae revealed with VLT/SPHERE-ZIMPOL and VLTI/AMBER. *Astron. Astrophys.* **589**, A91 (2016).
6. Ohnaka, K., Weigelt, G. & Hofmann, K.-H. Clumpy dust clouds and extended atmosphere of the AGB star W Hydrae revealed with VLT/SPHERE-ZIMPOL and VLTI/AMBER. II. Time variations between pre-maximum and minimum light. *Astron. Astrophys.* **597**, A20 (2017).
7. Takigawa, A., Kamizuka, T., Tachibana, S. & Yamamura, I. Dust formation and wind acceleration around the aluminum oxide-rich AGB star W Hydrae. *Sci. Adv.* **3**, eaao2149 (2017).
8. Vlemmings, W. et al. The shock-heated atmosphere of an asymptotic giant branch star resolved by ALMA. *Nat. Astron.* **1**, 848–853 (2017).
9. Khouri, T. et al. High-resolution observations of gas and dust around Mira using ALMA and SPHERE/ZIMPOL. *Astron. Astrophys.* **620**, A75 (2018).
10. Gottlieb, C. A. et al. ATOMIUM: ALMA tracing the origins of molecules in dust forming oxygen rich M-type stars. *Astron. Astrophys.* **660**, A94 (2022).
11. Wittkowski, M. et al. Aperture synthesis imaging of the carbon AGB star R Sculptoris. Detection of a complex structure and a dominating spot on the stellar disk. *Astron. Astrophys.* **601**, A3 (2017).
12. Paladini, C. et al. Large granulation cells on the surface of the giant star π^1 Gruis. *Nature* **553**, 310–312 (2018).
13. Leão, I. C., de Laverny, P., Mékarnia, D., de Medeiros, J. R. & Vandame, B. The circumstellar envelope of IRC+10216 from milli-arcsecond to arcmin scales. *Astron. Astrophys.* **455**, 187–194 (2006).
14. Stewart, P. N. et al. The weather report from IRC+10216: evolving irregular clouds envelop carbon star. *Mon. Not. R. Astron. Soc.* **455**, 3102–3109 (2016).
15. Siebert, M. A., Van de Sande, M., Millar, T. J. & Remijan, A. J. Investigating anomalous photochemistry in the inner wind of IRC+10216 through interferometric observations of HC_3N. *Astrophys. J.* **941**, 90 (2022).
16. Montargès, M. et al. A dusty veil shading Betelgeuse during its Great Dimming. *Nature* **594**, 365–368 (2021).
17. Ramstedt, S. et al. The circumstellar envelope around the S-type AGB star W Aql. *Astron. Astrophys.* **605**, A126 (2017).
18. Decin, L. et al. (Sub)stellar companions shape the winds of evolved stars. *Science* **369**, 1497–1500 (2020).
19. Freytag, B., Liljegren, S. & Höfner, S. Global 3D radiation-hydrodynamics models of AGB stars. Effects of convection and radial pulsations on atmospheric structures. *Astron. Astrophys.* **600**, A137 (2017).
20. Cernicharo, J., Marcelino, N., Agúndez, M. & Guélin, M. Molecular shells in IRC+10216: tracing the mass loss history. *Astron. Astrophys.* **575**, A91 (2015).
21. Sozzetti, A., Smart, R. L., Drimmel, R., Giacobbe, P. & Lattanzi, M. G. Evidence for orbital motion of CW Leonis from ground-based astrometry. *Mon. Not. R. Astron. Soc.* **471**, L1–L5 (2017).
22. Menten, K. M., Reid, M. J., Kamiński, T. & Claussen, M. J. The size, luminosity, and motion of the extreme carbon star IRC+10216 (CW Leonis). *Astron. Astrophys.* **543**, A73 (2012).
23. Weigelt, G. et al. 76mas Speckle-masking interferometry of IRC+10216 with the SAO 6m telescope: Evidence for a clumpy shell structure. *Astron. Astrophys.* **333**, L51–L54 (1998).
24. Chiavassa, A. & Freytag, B. 3D hydrodynamical simulations of evolved stars and observations of stellar surfaces. In *Proc. of a Conference at University Campus, Vienna, Austria on why galaxies care about AGB stars III: a closer look in space and time* (eds. by Kerschbaum, F. et al.) (Astronomical Society of the Pacific, 2015).
25. Höfner, S. & Freytag, B. Exploring the origin of clumpy dust clouds around cool giants. A global 3D RHD model of a dust-forming M-type AGB star. *Astron. Astrophys.* **623**, A158 (2019).
26. Martínez, L. et al. Prevalence of non-aromatic carbonaceous molecules in the inner regions of circumstellar envelopes. *Nat. Astron.* **4**, 97–105 (2020).
27. Cernicharo, J. et al. Discovery of SiCSi in IRC+10216: a missing link between gas and dust carriers of Si-C bonds. *Astrophys. J. Lett.* **806**, L3 (2015).
28. Decin, L. et al. ALMA data suggest the presence of spiral structure in the inner wind of CW Leonis. *Astron. Astrophys.* **574**, A5 (2015).
29. Guélin, M. et al. IRC+10216 in 3D: morphology of a TP-AGB star envelope. *Astron. Astrophys.* **610**, A4 (2018).
30. Ireland, M. J. & Scholz, M. Observable effects of dust formation in dynamic atmospheres of M-type Mira variables. *Mon. Not. R. Astron. Soc.* **367**, 1585–1593 (2006).
31. Norris, B. R. M. et al. A close halo of large transparent grains around extreme red giant stars. *Nature* **484**, 220–222 (2012).
32. Van de Sande, M. et al. Determining the effects of clumping and porosity on the chemistry in a non-uniform AGB outflow. *Astron. Astrophys.* **616**, A106 (2018).
33. Ridgway, S. & Keady, J. J. The IRC+10216 circumstellar envelope. II. Spatial measurements of the dust. *Astrophys. J.* **326**, 843 (1988).
34. Men'shchikov, A. B., Balega, Y., Blöcker, T., Osterbart, R. & Weigelt, G. Structure and physical properties of the rapidly evolving dusty envelope of IRC+10216 reconstructed by detailed two-dimensional radiative transfer modeling. *Astron. Astrophys.* **368**, 497–526 (2001).

Methods

ALMA millimetre-wavelength interferometric observations, calibration and reduction

The observations presented here correspond to ALMA project no. 2018.1.01485. They were carried out during two executions of 67 min each on 9 July 2019 at 17:26:15 (UTC) and on 10 July 2019 at 15:44:10 (UTC). Total integration time on IRC+10°216 was 68 min. The array was set into a configuration using 43 antennae that achieved 903 different baselines ranging between 111.2 m and 13.9 km (configuration c43-9). This configuration provided an angular resolution of around 20 mas and a maximum recoverable scale for the most extended emission of roughly 450 mas.

IRC+10°216 was observed at sky elevations ranging between 45° and 54° on 9 July 2019 and between 28° and 40° on 10 July 2019 through single-pointing integrations. On average the weather conditions were good, with an atmospheric precipitable water vapour content of approximately 1.2–2.1 mm, humidity between 10 and 25%, ambient temperatures below 2 °C and system temperatures between 80 and 180 K. Four spectral windows of 1.875 GHz bandwidth were centred at sky frequencies 264.901, 266.701, 249.901 and 251.701 GHz with spectral resolution of 0.55, 0.55, 0.59 and 0.58 km s^{-1}, respectively (nominal channel width is 488.281 kHz).

Calibration was performed with the standard pipeline of the Common Astronomy Software Applications (CASA) software package[35], and self-calibration and image synthesis with the Grenoble Image and Line Data Analysis Software (GILDAS) package. The bright calibrator J0854+2006 was observed to calibrate the bandpass and was also set for absolute flux reference, with flux of 2.61, 2.60, 2.69 and 2.68 Jy for each spectral window. Observations were carried out in single-polarization mode and only horizontal (H) polarization was observed. The flux calibration reference used is known to be polarized (A. Castro-Carrizo, private communication), although the CASA pipeline did not correct the adopted flux by the value corresponding to H polarization at the time of the observations. Due to this, a later correction of 7–10% was introduced in the data based on the polarization knowledge of the flux calibrator, also considering the hour angle during the observations (thanks to the Northern Extended Millimetre Array observatory database). Otherwise, the monitoring carried out by ALMA on the dates around the observations at different frequencies make these flux values very reliable (with uncertainty around 5% or less). J1002+1216 was observed every 2 min, to calibrate amplitude and phase gains over time.

The standard phase calibration was subsequently improved by self-calibration on the compact continuum emission of the source. Continuum results were obtained per baseband after line subtraction and then averaged to produce a single continuum map. Imaging restoration was performed with uniform weighting. The cleaning methods used during image synthesis were Hogbom[36] and Steer–Dewdney–Ito[37], where the latter is best suited to reducing clumpiness by the identification of clean component groups. The Steer–Dewdney–Ito method was used only for line emission imaging, and its results were assessed by comparison with the more standard Hogbom examples. The mean synthetic beam obtained for the different maps is 27 × 19 mas (with PA equal to 47°; further details can be seen in the caption of each figure).

Continuum main component fit and proper motion

The position of IRC+10°216, determined as the centre of the Gaussian fit to the bulk of the continuum emission, is $\alpha_{J2000.0}$ = 09 h 47 min 57.456 s ± 0.002 s and $\delta_{J2000.0}$ = + 13°.16′43″906 ± 0″033. The uncertainty of the position is the result of the addition in quadrature of the Gaussian fit uncertainty and one-fifth of the synthesized beam. The position uncertainty of interferometric observations can be approximated by roughly 0.5 θ_b/signal-to-noise ratio (SNR)—that is, beam size divided by ten for good SNR detection[38]—SNR ≥ 5. For observations with an extended configuration of the interferometer, as in is our case, accuracy

in the position is poorer than that amount by a factor of two due to atmospheric phase fluctuations. Therefore, we adopted a more conservative value for uncertainty as one-fifth of the half-power beamwidth synthesized beam. The integrated flux, within a square box of 400 mas length centred at the fitted position, amounted to 496 ± 11 mJy, of which some 90% corresponded to the bulk of the emission fitted by our Gaussian (see below). This flux compares well, considering the source variability, with previous measurements at similar wavelengths[29,39,40]. The peak intensity of our continuum source is 68.3 ± 2.4 mJy per beam with r.m.s. of the noise (1 σ level) equal to 92 μJy per beam. The fit to the continuum emission yields a major-axis FWHM of 56.0 ± 2.7 mas and a minor-axis FWHM of 49.9 ± 2.3 mas with a position angle of 58 ± 26°.

Highly accurate measurements of the position of IRC+10°216, carried out with the most extended configuration of the very large array, were presented and discussed by Menten et al.[22]. They reported the following coordinates for IRC+10°216: $\alpha_{J2000.0}$ = 09 h 47 min 57.4255 s ± 0.0006 s and $\delta_{J2000.0}$ = + 13°.16′43″815 ± 0″010, which represent an offset of $\Delta\alpha$ = 458 ± 31 mas and $\Delta\delta$ = 91 ± 34 mas with respect to our measured position. The time span between our observations and those of Menten et al.[22] is 13 years. Menten et al.[22] analysed available measurements of the position, leading to determination of a proper motion of 35 ± 1 and 12 ± 1 mas per year in right ascension and declination, respectively. Considering the time span, the proper motion of the source would match quite well with our right ascension but not with the declination, in which our 91 mas offset is significantly far from the 156 mas that one would expect even within uncertainties. A more in-depth investigation on this issue is beyond the scope of this paper, but we suggest that the mismatch might be a consequence of the resulting orbital motion of IRC+10°216, if it is part of a binary or multiple system, and differences in the parallax among observations registered in different epochs.

Continuum extended emission

We discuss here previous observations of continuum extensions at different infrared and optical wavelengths connected to the NE and NW extensions seen in our continuum map, which were also interpreted as dust patches expelled by IRC+10°216 and/or dust-embedded (sub) stellar companions. The radius of the stellar photosphere, as measured in the IR, is 19 mas—that is, approximately 2.5 AU[33,34]. We note, for conversion to physical scales, that the distance to IRC+10°216 was previously measured as 123 ± 14 pc[41]. It is also worth noting that these continuum infrared and optical studies yield only two-dimensional images whereas molecular line maps yield velocity information that can inform about wind acceleration and position along the line of sight of the expelled clumps.

Weigelt et al.[23] reported, from a 2 μm Speckle interferometry map with the 6 m Special Astrophysical Observatory, the presence of at least three dust clumps, the brightest of which is located at 200 mas NE and 140 NW from what they had assumed the star was. They argued that the matter ejection from the photosphere is inhomogeneous due to magnetic activity and large convection cells of size 0.8 R_* (ref. [42]). This result was followed up by time monitoring of IRC+10°216 in near infrared by Weigelt et al.[43]. These authors reported changes in the appearance of the dust shell when comparing different time periods, showing structural variations compatible with the movement and formation of new dust clumps. Monnier et al.[44] reported, from observations with the Berkeley Infrared Spatial Interferometer, an increase in size of the mid-infrared source by a factor of 2 over 10 years, which they interpreted as a sharp decrease in mass-loss rate, but it could be linked to the sporadic expulsion of clumps. Tuthill et al.[45] reported, from 2 μm Keck aperture-masking interferometry observations at four different epochs covering one pulsating cycle, the presence to the N and NE of the central source of four dusty knots moving outward at about 15 km s^{-1} molecular shell expansion velocity, perhaps indicating acceleration with increasing radius. Leão et al.[13,46] reported, from observations at 1.2 and 2.0 μm carried out with the Very Large Telescope Nasmyth

Article

Adaptative Optics System with an angular resolution of 70 mas, three bright clumps NW, N and NE of the central source, similar to those of our continuum image but located farther. Kim et al.[47] reported observations with the Hubble Space Telescope at three different epochs in 2001, 2011 and 2016, covering the wavelength range 5,800–9,800 Å, that show bright knots around the central star; one of the knots was tentatively identified as a companion star[48]. Nevertheless, this hypothesis has been dropped in their new study, in which it is assumed that the knots are dust knots illuminated by starlight through holes in the dusty inner envelope layers.

Chemical model

The chemical model is based on the code presented in Agúndez et al.[49]. We compute the chemical equilibrium composition of gas over a pressure–temperature parameter space relevant to the conditions of an AGB atmosphere (5×10^{-4}–5 mbar and 2,000–3,000 K). Chemical equilibrium is solved by minimization of the Gibbs free energy of the system. We considered 919 gaseous species, including atoms and molecules, with thermochemical data taken from different compilations and an elemental composition typical of C-rich AGB stars[49]. We show results only for the relevant molecules discussed in this work—that is, HCN, SiS and SiC_2—as well as the carbon dust precursor C_2 in Extended Data Figs. 3 and 4.

Shocks, outflows and binarity

The occurrence of shocks in the extended atmospheres of AGB stars is thought to exist as a consequence of the interplay between stellar pulsation and the convective motions of material in the outermost shells of the star[8,25]. The periodic ejection of material leads to the creation of a dynamical atmosphere where infalling material that is still gravitationally bound to the star could encounter recently ejected material, causing temperature and density enhancements across the stellar atmosphere. We calculated the molecular emission of IRC+10°216 with the aid of the radiation transfer code MADEX[50] for a time-dependent envelope model that includes stellar pulsation. This envelope model is based on the output of the models presented by Cherchneff[51], in which physical conditions and chemical abundances were computed at different pulsation phases. Shocks produced by the pulsation movement of the star lift outwards the gas layers close to the stellar surface and then the material falls back due to stellar gravity after the shock passage. The effect of shocks should be seen in the line profiles at the current angular resolution of 20 mas as narrow features occurring at very specific velocities (Extended Data Fig. 5). These narrow emission and absorption features appear due to a combination of effects that include the amount of gas and its relative position, velocity and temperature. However, as we show in Extended Data Figs. 6 and 7, the observed line profiles along different strips through the stellar atmosphere lack any supporting evidence of shocks in any of the species analysed. Nevertheless, we cannot rule out the existence of shocks that are not seen in our data due to effects such as excitation, gas turbulence and opacity effects, or in the case that they are smoothed in our data due to insufficient resolution. In Extended Data Figs. 8 and 9 we also show different patterns of emission and absorption depending on the line of sight where no signatures of shocks are seen. Inside the stellar disk we see molecular absorption lines as a consequence of absorption against the stellar continuum and self-absorption. Between the photosphere and radio photosphere we observe little or no emission and absorption. Finally, as we look beyond the radio photosphere, only molecular emission is seen.

On the other hand, we also investigated whether there is any emergent bipolar or collimated outflow noticeable in the position–velocity diagrams along different directions. Such outflow would most probably be caused by a binary companion orbiting the AGB star, as suggested in the formation scenarios of preplanetary nebulae[52]. The presence of a binary companion has been argued as explaining different signatures seen in the circumstellar shells of IRC+10°216, such as off-centred shells and spiral structure[20,28,53]. Kim et al.[48] reported the detection of a point-like source in HST images lying 0."5 to the SE from IRC+10°216 that could be the companion star. Different studies have reported an elongation along the NE–SW direction of IRC+10°216's envelope, which would mark a preferential direction or have a role of symmetry axis, and the observation of bright infrared clumps moving in this direction[45,54] (and references therein). This has led to suggestions that IRC+10°216, which is known to be a star in the latest stages of the AGB phase, is already evolving towards a preplanetary nebula and starting a bipolar outflow due to the presence of a binary companion. Such an outflow would certainly break the symmetry and homogeneity of the stellar wind. Nevertheless, we have found no evidence in our data of outflows, disk or torus-like structures, or preferred ejection directions.

Decin et al.[28] presented subarcsecond resolution (roughly 0."5) ALMA data of IRC+10°216 in which they suggest the presence of spiral structure in its inner wind. We can directly compare that with our maps of HCN in the main text, in which a more complex structure is seen. A clear spiral pattern with complete arms is not seen, but some blobs or clumps are patently visible. Our maps show a much more complex situation in which different molecules trace different structures. At atmospheric level it is hard to interpret the spatial distribution of SiS, HCN and SiC_2 seen in our data as a sole consequence of the presence of a companion.

Hydrodynamical models of the interplay between an AGB star and a binary companion[55,56] showed a recognizable degree of symmetry in the patterns generated in the circumstellar material that we did not observe. Decin et al.[28] also presented a three-dimensional (3D) model of the envelope with a binary companion in which several parameters related to the orbital properties of the system were tested. From their analysis, they ruled out the possibility of a Jupiter-like or brown dwarf secondary based on arcsec-scale signatures in the position–velocity diagrams. However, they assumed a relatively high mass of 4 $M_\odot$ for IRC+10°216 but more recent estimates based on oxygen isotopic ratios indicated a mass of 1.6 $M_\odot$ (ref. [57]). Kim and Taam[58] explored the impact of wide binaries on the morphology of AGB circumstellar envelopes. These models predict the emergence of a spiral pattern that can be seen as a ring-like pattern if the system is observed edge-on (inclination of 90°), which seems incompatible with the large-scale morphology of IRC+10°216's circumstellar envelope[20,29]. Malfait et al.[59] also presented smooth-particle hydrodynamic models of binary interaction with AGBs. They explored models of a 1.5 $M_\odot$ AGB accompanied by a 1 $M_\odot$ star at 6 AU (semimajor axis). The secondary induces a motion of the stars around the centre of mass of the system while generating a spiral shock, and perturbs the AGB wind material. Different patterns can be observed in their models, from perfect spirals to more irregular configurations, but none of their simulations resemble our observations. Moreover, it would still be very difficult to reconcile the predicted density profile with the chemical segregation that we observed. Similar models were also presented by Maes et al.[60]. Recently, Aydi & Mohamed[61] presented 3D hydrodynamical models of the circumstellar environments of evolved stars affected by the presence of nearby substellar companions. They concluded that if the companion is at a distance greater than four stellar radii a single spiral arm should be seen, which can be ruled out from our data. For a much closer separation to the companion a more complex structure of multiple spirals is observed, whose configuration depends on many orbital and system parameters that were explored. Nevertheless, we note again that stellar outflow at the atmospheric level is not an isotropic wind, as can be seen in the images we present. These authors discussed the models of Freytag et al.[19], which show that convection cells and fundamental-mode pulsation will result in chaotic shock wave structures around the AGB star, shifting from spherical symmetry. These structures cause anisotropies in the temperature and density conditions leading to chemical variations in the gas depending on the angle (direction) from the centre of

the star. We propose that such chaotic structures cause the chemical anisotropies seen in our maps and that, in combination with interaction with a binary companion, shape the circumstellar envelope of this archetypal AGB.

To test whether blobs launched from the photosphere along random directions can explain our observations, we developed several models based on the evolving envelope model presented by Cernicharo et al.[20]. Because our code is flexible, it can be used to model an isolated star or a binary system involving an AGB star with different physical and orbital parameters such as masses, inclination and period, among others. The envelope is formed by a modulated ejection of matter in a spherical wind that simulates the pulsation-driven outflow in AGB stars—that is, the steady-state wind. Different contrasts between minima and maxima in the pulsation stage (up to 100) and different periods (up to 3 years) were tested. The main development of the model is that the AGB steady-state wind is modified by discrete spherical caps that are randomly ejected. These spherical caps were modelled as temporary enhancements of wind density at the photosphere, keeping constant any other physical or chemical quantity for the sake of simplicity. These caps were centred at random positions across the photosphere with a formation rate probability typically lower than 10–30% and a typical angular width of 60°. The formation of each cap lasts about 2.5 months and only one cap is formed at a time. The time evolution of the system is calculated over a period of time and the radiation transfer problem is solved for the CO $J = 2$–1 line, assuming local thermodynamic equilibrium to simplify calculations. Finally, the maps produced were convolved with a Gaussian beam to simulate the constraints imposed by interferometers on observations. We checked with the CASA modelling tool 'simalma' that the array configuration does not significantly modify the region of the envelope explored in the current work. We note that the code aims to provide qualitative information about the formation of structures in the envelope. More accurate studies are beyond the scope of the current work. The resulting models can be seen in Extended Data Fig. 10.

First, we developed a 'control' model, a scenario that should represent the case of an isolated AGB star with a steady-state wind (see case a in Extended Data Fig. 10). This model generates a smooth, circularly symmetric brightness distribution with decaying emission with distance to the star besides the absorption in the innermost region. In the second scenario we add the presence of a close companion based on the basic parameters presented by Decin et al.[28]—that is, an inclination of 60°, separation of 25 AU and masses of 4 $M_{\odot}$ for the AGB and 1.1 $M_{\odot}$ for the companion (case b in Extended Data Fig. 10). In this case a smooth, circularly symmetric outflow was observed in the innermost region of the envelope map plus a spiral pattern that is generated in the presented image at the northeast and continues revolving clockwise. We note that we explored a large parameter space including different masses for the AGB and the companion, separation between the stars and the inclination of the system. None of these models produces the arcs and blobs we observed in maps of circumstellar emission: these features appear only under a different scenario, the third case (case c in Extended Data Fig. 10), which adds randomly ejected blobs to AGB outflow. These models generate random blobs at the stellar photosphere that leave anisotropic features in the emission maps with a marked resemblance to those seen in the ALMA maps, such as the two blobs to the west in Extended Data Fig. 10c. Moreover, arcs are also observed in these models as a consequence of the evolution of the launched blobs and interaction with circumstellar material. In this case we shortened the distance between the stars to 10 AU to maintain the value of the orbital period as low as possible, considering that the kinematic age of the random ejections is a few years only. The spiral structure due to the binary companion is not always clearly seen, probably as a consequence of the interaction of blobs with the material trail. Nevertheless, we recall that we have not seen any spiral pattern in the observed emission maps. Modifications of pulsation contrast between shells and the pulsation

period for values under 3 years do not change the results. We note that the infrared light period of IRC+10°216 is about 1.8 years and, in such case, any high-contrast shell is smoothed out in the outflow by the angular resolution provided by ALMA. Considering a gas expansion velocity of approximately 5 km s^{-1} close to the photosphere, an angular resolution as high as 7 mas should be necessary for this task. Following this analysis, we can conclude that the anisotropic features appear only if the ejection of blobs is included in the models.

Data availability

All the observational products used here are public and available through the ALMA, SMA and IRAM-30m archives:https://almascience.nrao.edu/aq/https://lweb.cfa.harvard.edu/cgi-bin/sma/smaarch.plhttps://iram-institute.org/science-portal/data-archive/.

Code availability

The 2012 version of the MADEX code, including spectroscopic information for approximately 3,500 species, is available as an executable in https://nanocosmos.iff.csic.es/madex/. The chemical equilibrium and evolving envelope models are available on request. Enquiries about codes can be addressed to the corresponding authors and to the developers of the codes: M.A. for the chemical code, J.C. for the MADEX code and J.C. and J.P.F. for models of the evolving envelope.

35. McMullin, J. P., Waters, B., Schiebel, D., Young, W. & Golap, K. CASA architecture and applications. *Publ. Astron. Soc. Pac.* **376**, 127 (2007).
36. Högbom, J. A. Aperture synthesis with a non-regular distribution of interferometer baselines. *Astron. Astrophys. Suppl.* **15**, 417 (1974).
37. Steer, D. G., Dewdney, P. E. & Ito, M. R. Enhancements to the deconvolution algorithm 'CLEAN'. *Astron. Astrophys.* **137**, 159–165 (1984).
38. Reid, M. J. et al. The distance to the center of the galaxy: H 2O maser proper motions in Sagittarius B2(N). *Astrophys. J.* **330**, 809 (1988).
39. Lucas, R. 1.3 MM Plateau de Bure observations of IRC+10216. *Astrophys. Space Sci.* **251**, 247–250 (1997).
40. Fonfría, J. P. et al. The complex dust formation zone of the AGB star IRC+10216 probed with CARMA 0.25 arcsec angular resolution molecular observations. *Mon. Not. R. Astron. Soc.* **445**, 3289–3308 (2014).
41. Groenewegen, M. A. T. et al. An independent distance estimate to CW Leonis. *Astron. Astrophys.* **543**, L8 (2012).
42. Freytag, B., Holweger, H., Steffen, M. & Ludwig, H.-G. On the scale of photospheric convection. In *Proc. of the ESO workshop: Science with the VLT Interferometer* 316 (Springer, 1997).
43. Weigelt, G. et al. Bispectrum speckle interferometry of IRC+10216: the dynamic evolution of the innermost circumstellar environment from 1995 to 2001. *Astron. Astrophys.* **392**, 131–141 (2002).
44. Monnier, J. D. et al. Mid-infrared interferometry on spectral lines. II. Continuum (dust) emission around IRC+10216 and VY Canis Majoris. *Astrophys. J.* **543**, 861–867 (2000).
45. Tuthill, P. G., Monnier, J. D., Danchi, W. C. & Lopez, B. Smoke signals from IRC+10216. I. Milliarcsecond proper motions of the dust. *Astrophys. J.* **543**, 284–290 (2000).
46. Leão, I. C., de Laverny, P., Mekarnia, D., de Medeiros, J. R. & Vandame, B. Observations of the AGB star IRC+10216 from milliarcsec to arcmin spatial scales. *Publ. Astron. Soc. Pac.* **378**, 309 (2007).
47. Kim, H. et al. Multiepoch optical images of IRC+10216 tell about the central star and the adjacent environment. *Astrophys. J.* **914**, 35 (2021).
48. Kim, H., Lee, H.-G., Mauron, N. & Chu, Y.-H. HST images reveal dramatic changes in the core of IRC+10216. *Astrophys. J. Lett.* **804**, L10 (2015).
49. Agúndez, M., Martínez, J. I., de Andres, P. L., Cernicharo, J. & Martín-Gago, J. A. Chemical equilibrium in AGB atmospheres: successes, failures, and prospects for small molecules, clusters, and condensates. *Astron. Astrophys.* **637**, A59 (2020).
50. Cernicharo, J. Laboratory astrophysics and astrochemistry in the Herschel/ALMA era. *EAS Publ. Ser.* **58**, 251–261 (2012).
51. Cherchneff, I. The inner wind of IRC+10216 revisited: new exotic chemistry and diagnostic for dust condensation in carbon stars. *Astron. Astrophys.* **545**, A12 (2012).
52. Soker, N. Binary progenitor models for bipolar planetary nebulae. *Astrophys. J.* **496**, 833–841 (1998).
53. Guelin, M., Lucas, R. & Cernicharo, J. MgNC and the carbon-chain radicals in IRC+10216. *Astron. Astrophys.* **280**, L19–L22 (1993).
54. Velilla-Prieto, L. et al. IRC+10°216 mass loss properties through the study of λ 3 mm emission. Large spatial scale distribution of SiO, SiS, and CS. *Astron. Astrophys.* **629**, A146 (2019).
55. Mastrodemos, N. & Morris, M. Bipolar preplanetary nebulae: hydrodynamics of dusty winds in binary systems. I. Formation of accretion disks. *Astrophys. J.* **497**, 303–329 (1998).
56. Mastrodemos, N. & Morris, M. Bipolar pre-planetary nebulae: hydrodynamics of dusty winds in binary systems. II. Morphology of the circumstellar envelopes. *Astrophys. J.* **523**, 357–380 (1999).

Article

57. De Nutte, R. et al. Nucleosynthesis in AGB stars traced by oxygen isotopic ratios. I. Determining the stellar initial mass by means of the 17O/18O ratio. *Astron. Astrophys.* **600**, A71 (2017).
58. Kim, H. & Taam, R. E. Wide binary effects on asymmetries in asymptotic giant branch circumstellar envelopes. *Astrophys. J.* **759**, 59 (2012).
59. Malfait, J. et al. SPH modelling of wind-companion interactions in eccentric AGB binary systems. *Astron. Astrophys.* **652**, A51 (2021).
60. Maes, S. et al. Route towards complete 3D hydro-chemical simulations of companion-perturbed AGB outflows. In *Proc. of the International Astronomical Union on the Origin of Outflows in Evolved Stars* (eds. Decin, L. et al.) (Cambridge Univ. Press, 2021).
61. Aydi, E. & Mohamed, S. 3D models of the circumstellar environments of evolved stars: formation of multiple spiral structures. *Mon. Not. R. Astron. Soc.* **513**, 4405–4430 (2022).

Extended Data Fig. 1 | Velocity-integrated emission maps of SiS isotopologues in different vibrationally excited states. The velocity-integrated emission maps are shown in colour scale. Note that the intensity scale varies within boxes for improved visualisation. The grey contours correspond to 10, 30, 50, 100, 200, 300, 400, 500, and 600 σ of the r.m.s. of the noise of the continuum emission, which is equal to 92 μJy beam^{-1}. The cyan dashed contour represents the radio photosphere[22]. The shape of the synthetic beam is shown in the bottom-left corner of each box. North is up, and East to the left.
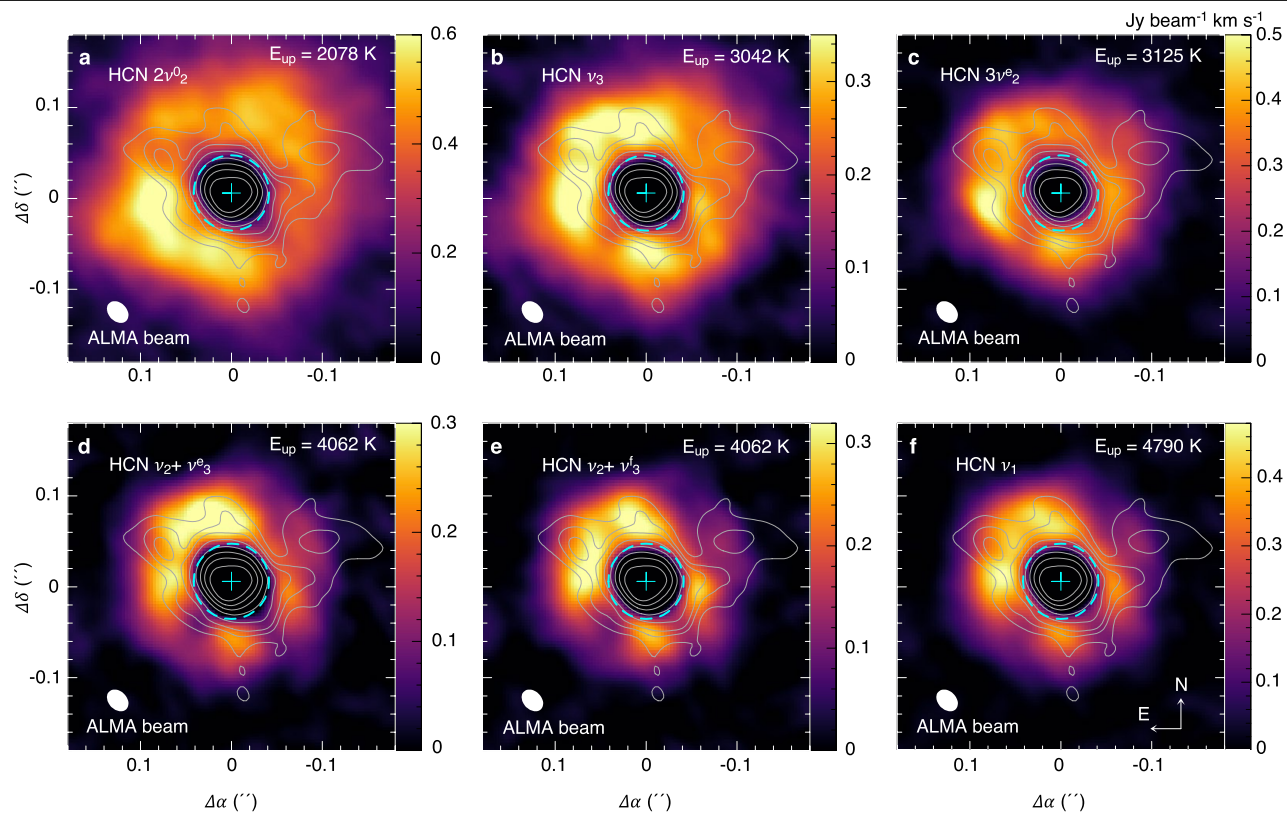
Extended Data Fig. 2 | Velocity-integrated emission maps of HCN isotopologues in different vibrationally excited states. The colour scale, contours, beam, and orientation are defined as in Extended Data Fig. 1.
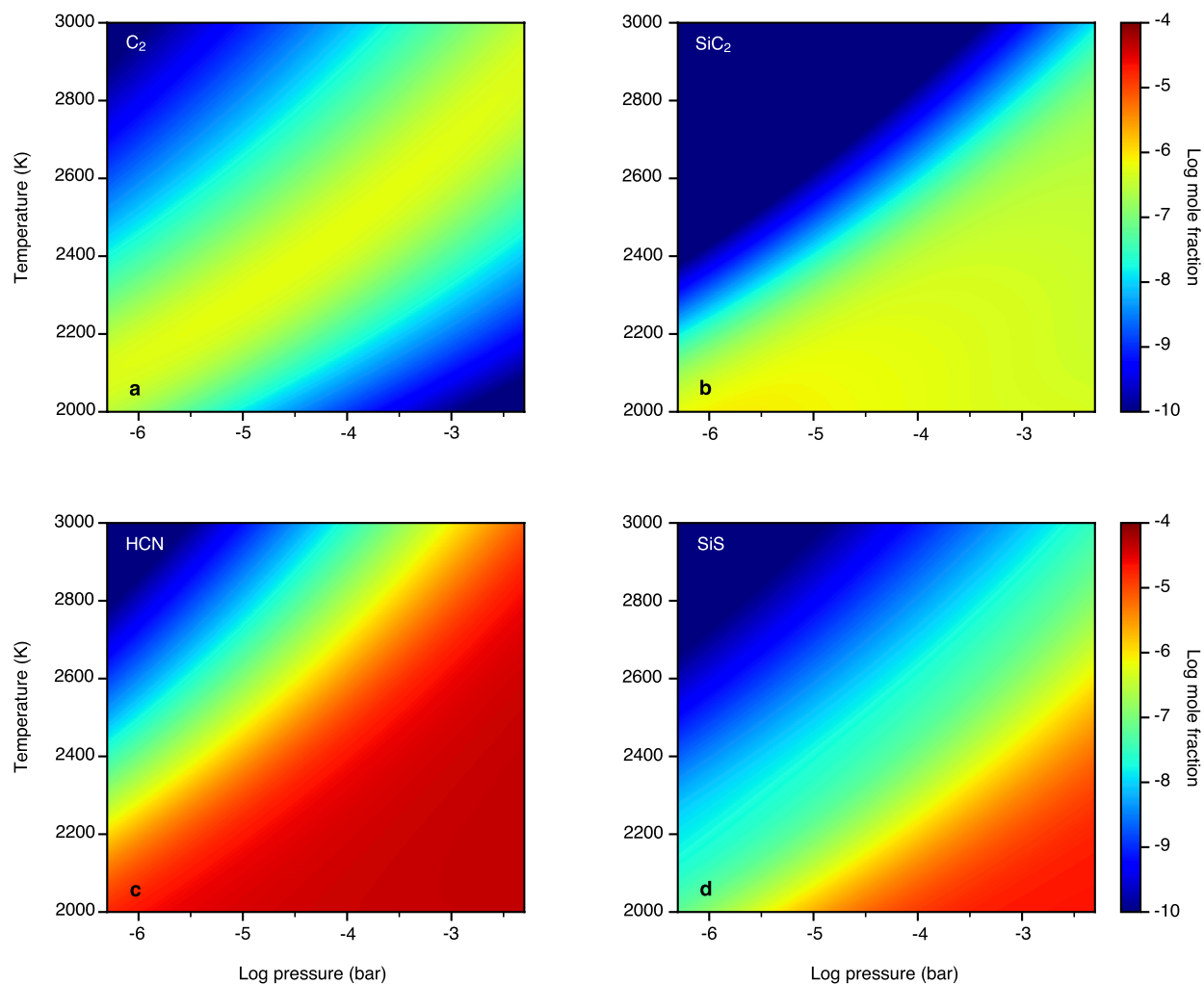
Extended Data Fig. 3 | Results from the chemical equilibrium models for C₂, SiC₂, HCN, and SiS. The colour scale map represents the logarithm of the mole fraction of the given molecule as a function of the kinetic temperature and the logarithm of the pressure of the gas.
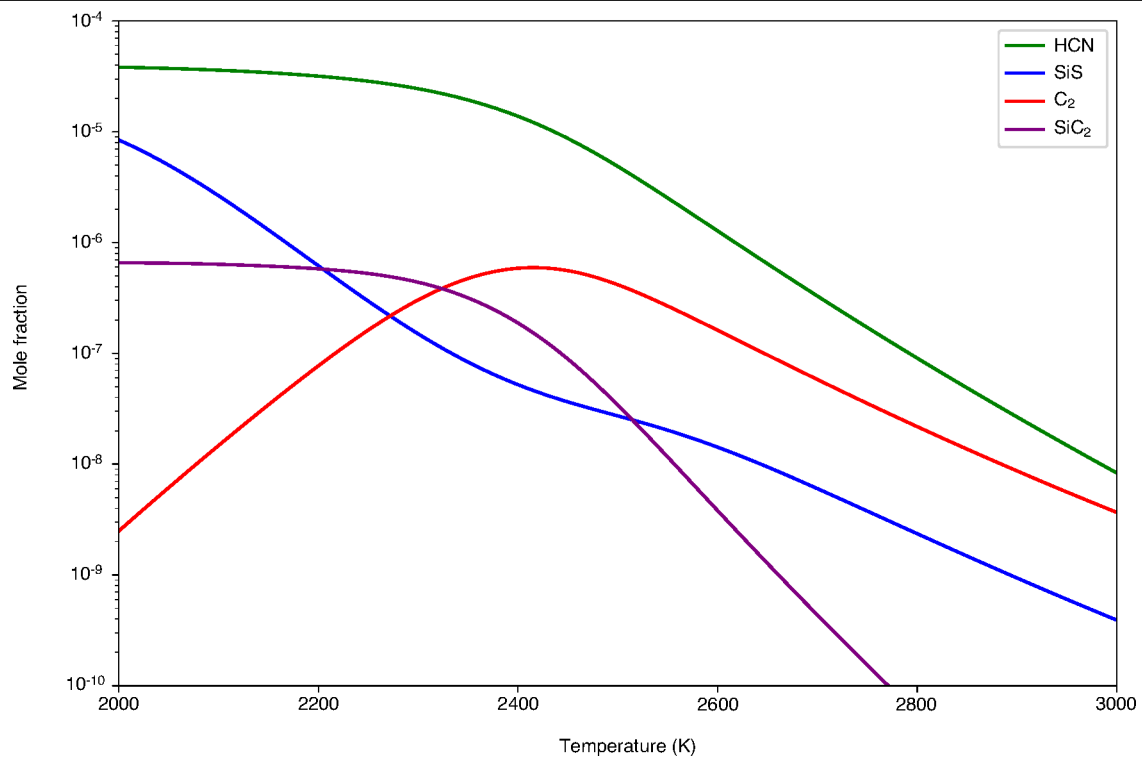
Extended Data Fig. 4 | Fractional abundance profiles. The abundance profiles are shown as a function of temperature for a fixed pressure of 5×10^{-5} bar, which should be close to the gas pressure at the photosphere of IRC+10°216 ref. [49].
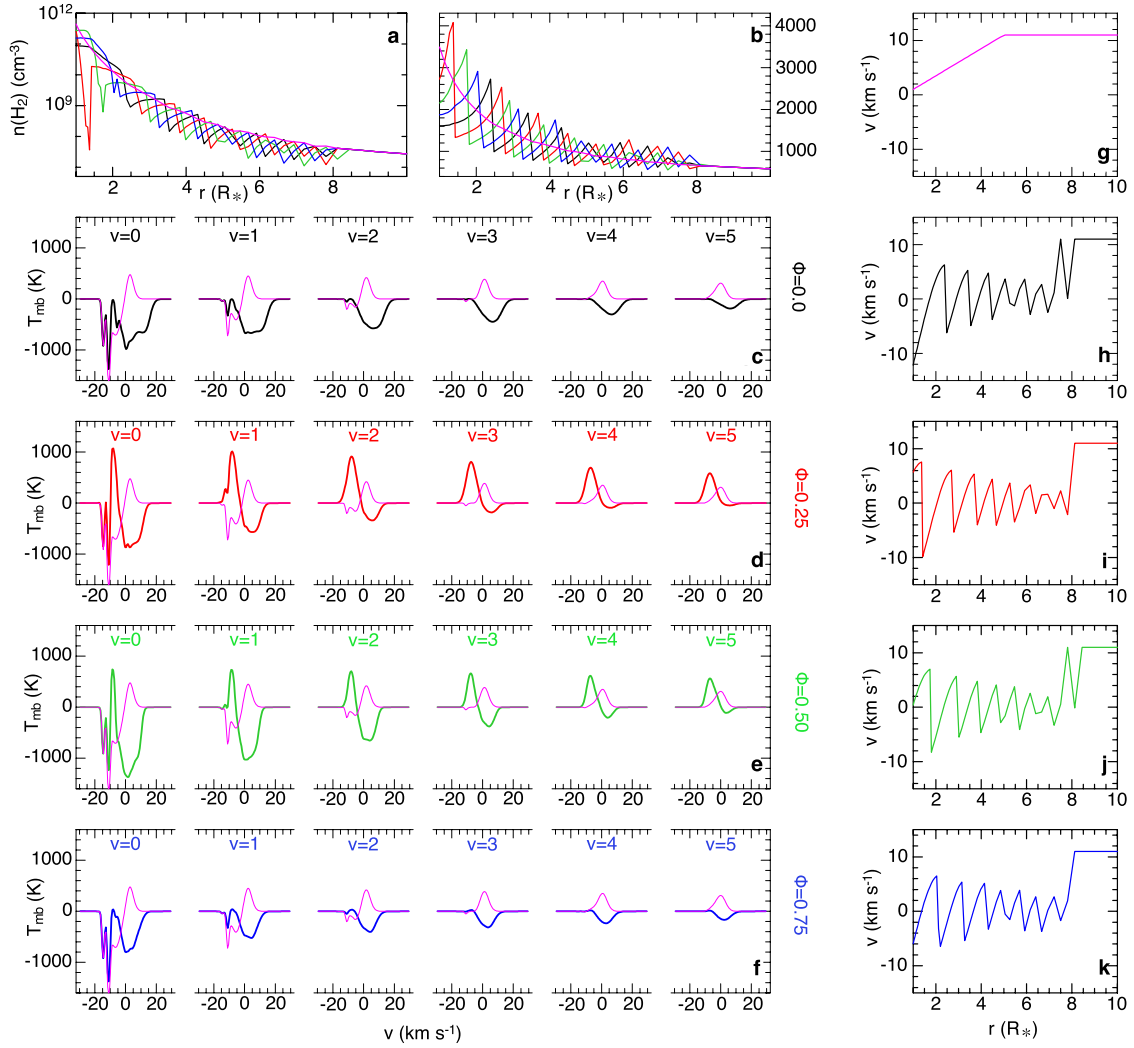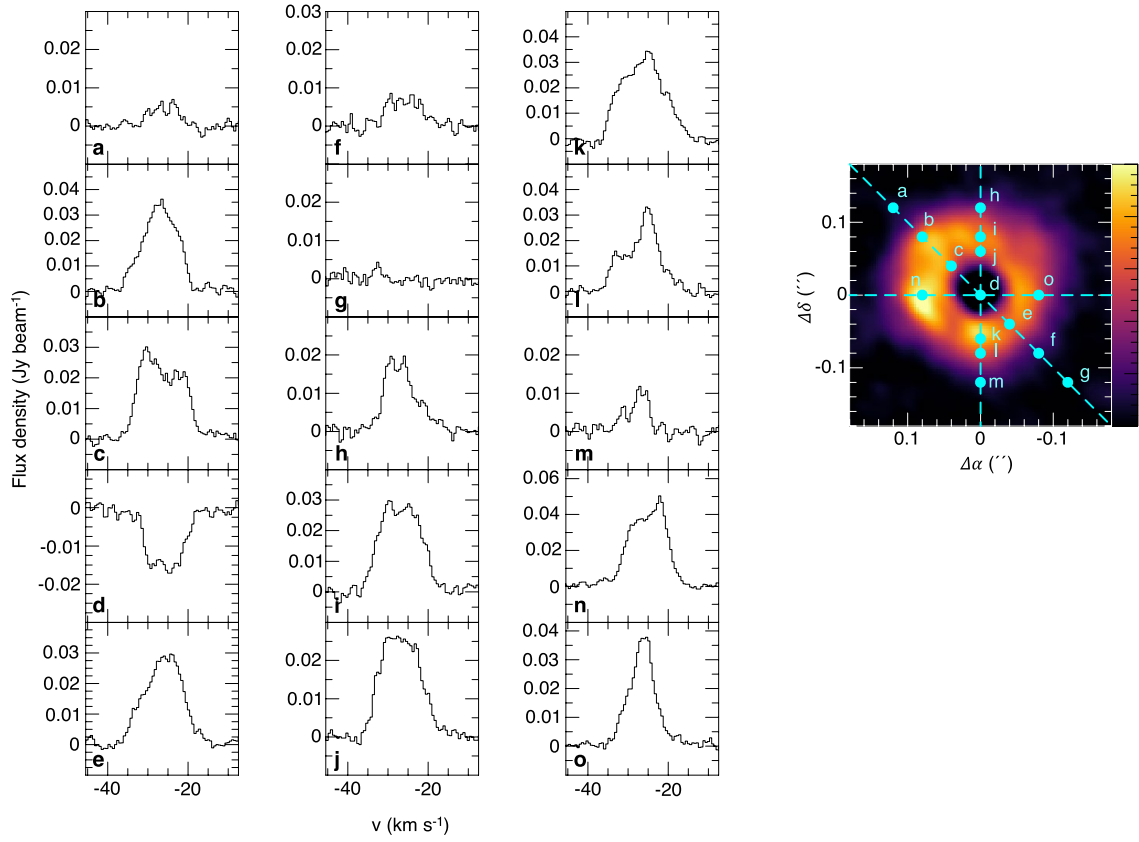
Extended Data Fig. 5 | Predicted line profiles of the $J = 14$–13 SiS line in different vibrational states as a function of the pulsation phase. a–b: density and temperature profiles, where oscillating lines represent the phases $\phi = 0$ (black), $\phi = 0.25$ (red), $\phi = 0.5$ (green), and $\phi = 0.75$ (blue). An additional model with no stellar pulsation using density and temperature profiles that falls as r^{-2} and $r^{-0.7}$, respectively, is shown as a pink (non-oscillating) solid line. **c–f:** Emergent line profiles where the coloured lines, which follow the colour code mentioned before, represent the predictions for an angular resolution of 0″.2. **g–h:** Velocity profile of the gas following also this colour code.
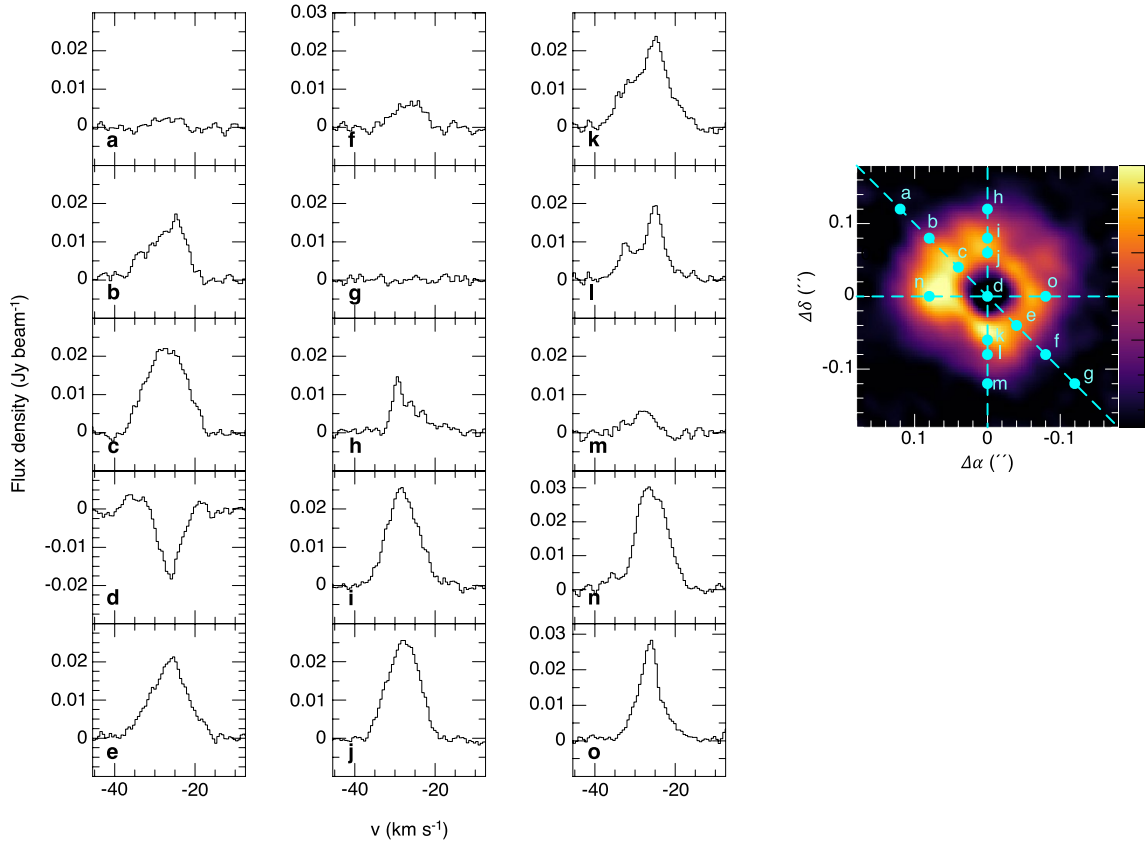
Extended Data Fig. 6 | Line profiles of the $v = 2$ $J = 14$–13 SiS line as observed at different locations in the plane of the sky. The lines have been obtained by averaging the spectra in an area of 10 mas surrounding each selected position. The different numbered offset positions are shown and numbered in the total intensity map to the right. Each corresponding position number is shown in red at the bottom-left corner of the boxes displaying the plots of the spectra.

Extended Data Fig. 7 | Line profiles of the HCN $3\nu_2^e\,J=3-2$ line as observed at different locations in the plane of the sky. Details of this figure are defined as in Extended Data Fig. 6.
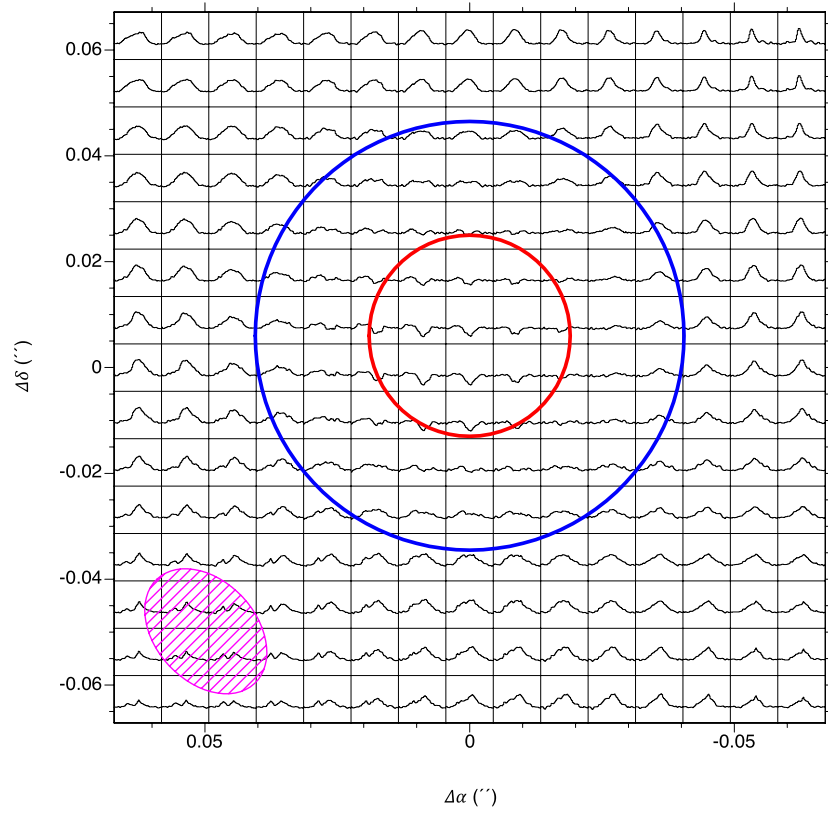
Extended Data Fig. 8 | Spectra in velocity units at different offsets from the source of the SiS $v = 2$ $J = 14$–13 line. The velocity range shown for each spectrum is ± 15 km s^{-1} with respect to the systemic velocity of the source, from negative (left) to positive (right). The intensity scale, in Jy beam^{-1}, ranges between -0.03 and 0.06. The red circle represents the stellar disk in the IR (radius equal to 19 mas)[33], while the blue circle correspond to the radio photosphere (radius equal to 40.5 mas)[22].
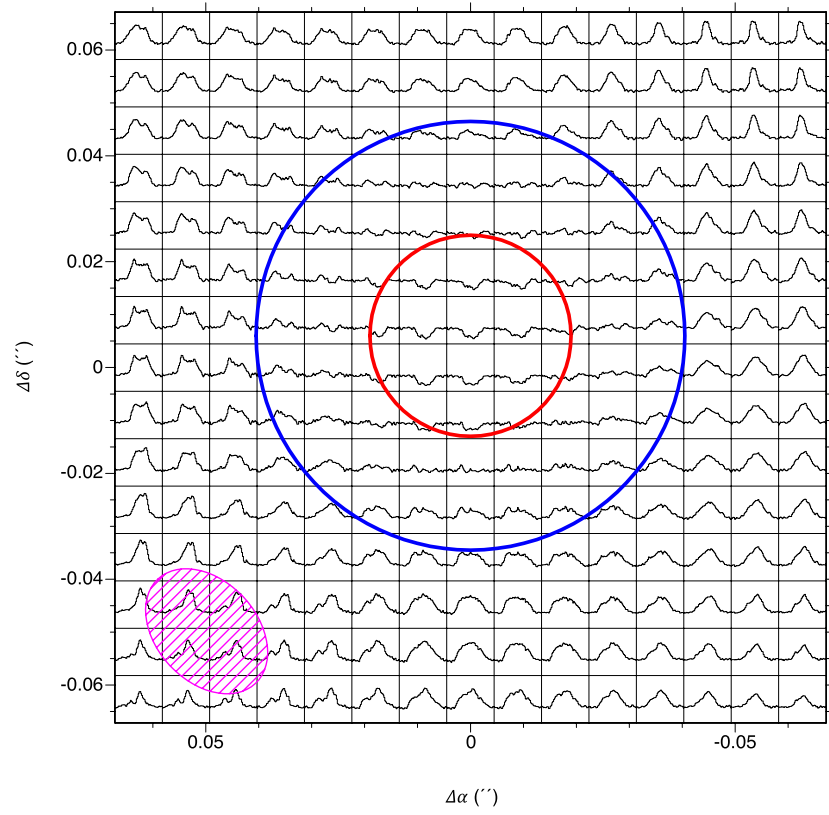
Extended Data Fig. 9 | Spectra in velocity units at different offsets from the source of the HCN $3\nu_2^e$ line. Details of this figure are defined as in Extended Data Fig. 8.
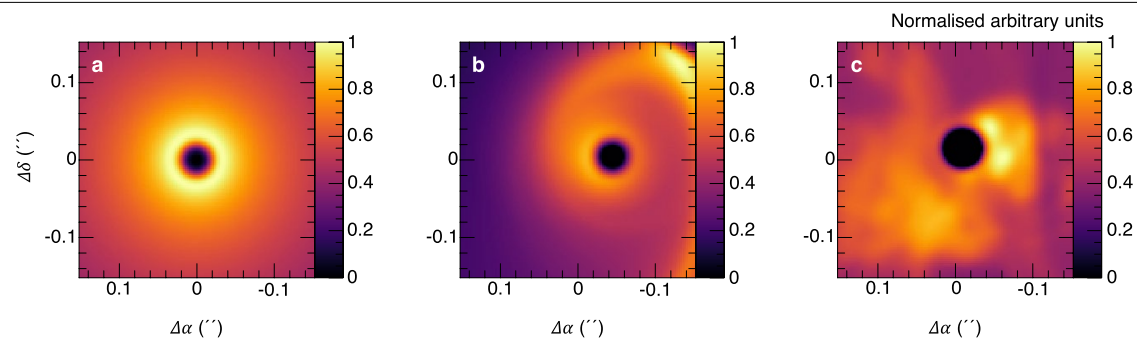
Extended Data Fig. 10 | Results from the growing envelope model. Three cases are presented: a) control case of an isolated AGB star without formation of blobs, b) AGB steady wind in a binary system with an inclination of 60° separated by 25 AU, and c) as in b but for a closer companion located at 10 AU and including the randomly generated blobs at the AGB stellar photosphere. The maps are in normalised intensity units to their respective maximum intensity.